

Search for hidden-photon cold dark matter using a K-band cryogenic receiver

N. Tomita^a S. Oguri,^{b,1} Y. Inoue,^c M. Minowa,^{a,d} T. Nagasaki,^e
J. Suzuki,^f O. Tajima,^f

^aDepartment of Physics, School of Science, The University of Tokyo, 7-3-1 Hongo, Bunkyo-ku, Tokyo 113-0033, Japan

^bInstitute of Space and Astronautical Science (ISAS), Japan Aerospace Exploration Agency (JAXA), 3-1-1 Yoshinodai, Chuo-ku, Sagami-hara, Kanagawa 252-5210, Japan

^cInternational Center for Elementary Particle Physics, The University of Tokyo, 7-3-1 Hongo, Bunkyo-ku, Tokyo 113-0033, Japan

^dResearch Center for the Early Universe (RESCEU), School of Science, The University of Tokyo, 7-3-1 Hongo, Bunkyo-ku, Tokyo 113-0033, Japan

^eInstitute of Particle and Nuclear Studies, High Energy Accelerator Research Organization (KEK), 1-1 Oho, Tsukuba, Ibaraki 305-0801, Japan

^fDepartment of Physics, Faculty of Science, Kyoto University, Kitashirakawa Oiwake-cho, Sakyo-ku, Kyoto, 606-8502, Japan

E-mail: tomita@icepp.s.u-tokyo.ac.jp, oguri.shugo@jaxa.jp,
berota@icepp.s.u-tokyo.ac.jp, minowa.phys@gmail.com, tnaga@post.kek.jp,
suzuki.junya.4r@kyoto-u.ac.jp, tajima.osamu.8a@kyoto-u.ac.jp

Abstract. We search for hidden-photon cold dark matter (HP-CDM) using a spectroscopic system in a K-band frequency range. Our system comprises a planar metal plate and cryogenic receiver. This is the first time a cryogenic receiver has been used in the search for HP-CDM. Such use helps reduce thermal noise. We recorded data for 9.3 hours using an effective aperture area of 14.8 cm^2 . No signal was found in the data. We set upper limits for the parameter of mixing between the photon and HP-CDM in the mass range from 115.79 to $115.85 \text{ } \mu\text{eV}$, $\chi < 1.8\text{--}4.3 \times 10^{-10}$, at a 95% confidence level. This is the most stringent upper limit obtained to date in the considered mass range.

Keywords: dark matter detectors, dark matter experiments, particle physics - cosmology connection

¹Corresponding author.

Contents

1	Introduction	1
2	Experimental setup	2
3	Data set	4
4	Calibration	4
5	Analysis	7
6	Results	9
7	Conclusions	10

1 Introduction

Various astronomical observations support the existence of cold dark matter (CDM). In particular, they show that CDM localizes in galaxy halos as non-relativistic matter. We understand that the gravity of galaxies is dominated by CDM. However, we do not know whether CDM interacts with standard-model particles except through gravity. A weakly interacting massive particle is a popular candidate of CDM, and it is expected to have heavy mass (more than a GeV in typical models). Many experiments have made efforts towards its detection. However, there has not yet been any conclusive result [1–6]. In recent years, another theoretical candidate, the weakly interacting slim particle, has been suggested. The weakly interacting slim particle is expected to have a very small mass [7, 8]. The hidden photon (HP) is a candidate weakly interacting slim particle and is a U(1) gauge boson that kinetically mixes with ordinary photons [9]. The effective Lagrangian in this model is

$$\mathcal{L} = -\frac{1}{4}F_{\mu\nu}F^{\mu\nu} - \frac{1}{4}\tilde{X}_{\mu\nu}\tilde{X}^{\mu\nu} - \frac{1}{2}\chi F_{\mu\nu}\tilde{X}^{\mu\nu} + \frac{1}{2}m_{\gamma'}^2\tilde{X}_\mu\tilde{X}^\mu, \quad (1.1)$$

where $F_{\mu\nu}$ is the field strength of the electromagnetic field, $\tilde{X}_{\mu\nu}$ is the field strength of the HP field (\tilde{X}^μ), $m_{\gamma'}$ is the mass of the HP, and χ is the coupling constant of kinetic mixing. The HP as CDM (hereafter HP-CDM) has been searched for via the kinetic mixing term (i.e., the third term in the above equation). Thus far, experiments conducted using cavities have given strong upper limits at a mass below 20 μeV [10].

A methodology of searching for HP-CDM in the higher mass region has been suggested [11]. Kinetic mixing converts HP-CDM into the electromagnetic waves (i.e., photons) at the surface of a metal plate. The frequency of the conversion photon (ν_0) represents the mass of the HP ($m_{\gamma'}$),

$$h\nu_0 = m_{\gamma'}c^2, \quad (1.2)$$

where h and c are respectively the Planck constant and speed of light. The original proposal suggested the use of a spherical metal plate for concentrating conversion photons whereas a recently published paper suggested combining a planar plate and parabolic mirror [12].

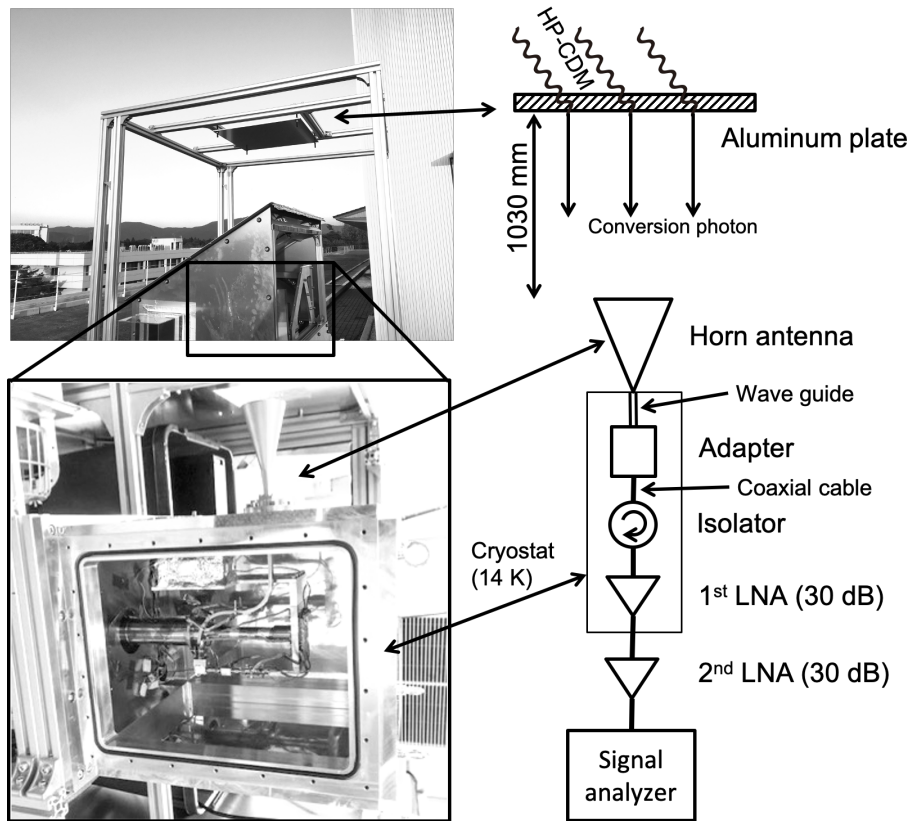


Figure 1. Overview of the experimental setup.

In experiments using a plate, the mixing angle χ is determined as described in ref. [11],

$$\chi = 4.5 \times 10^{-14} \left(\frac{P_{\gamma'}}{10^{-23} \text{ W}} \right)^{1/2} \left(\frac{1 \text{ m}^2}{A_{\text{eff}}} \right)^{1/2} \left(\frac{0.3 \text{ GeV/cm}^3}{\rho_{\text{CDM,halo}}} \right)^{1/2} \left(\frac{\sqrt{2/3}}{\alpha} \right), \quad (1.3)$$

where $P_{\gamma'}$ is the measured power of the conversion photon, A_{eff} is the effective area of the antenna, $\rho_{\text{CDM,halo}}$ is the CDM density around the Solar System ($0.39 \pm 0.03 \text{ GeV/cm}^3$ [13]), and α is a factor determined by the angular distribution of the HP-CDM field relative to the sensitive polarization axis. For experiments using a single-polarization detector, we chose $\alpha = \sqrt{1/3}$ in the case of a random distribution [7]. The sensitivity of the HP-CDM search depends on A_{eff} and a detection limit of power, $P_{\gamma'} = NEP/\sqrt{t}$, where NEP is the noise equivalent power of the system while t is the data integration time.

In this paper, we search for the HP-CDM using a planar plate and a receiver. The detection principle is the same as that in ref. [12]. We focus on improving the NEP using a cryogenic receiver. We describe the experimental setup in section 2, respectively describe the data set and calibrations in sections 3 and 4, present the analysis method in section 5, give search results in section 6, and present conclusions in section 7.

2 Experimental setup

Our system comprises an aluminum plate and a cryogenic receiver operating in the K-band as illustrated in Figure 1. HP-CDM converts the photon at the surface of the aluminum

Table 1. Information on parts shown in Figure 1.

Aluminum plate	500 mm × 500 mm × 6 mm, A5052-H112
Horn antenna	Millitech, SGH-42-SC000, circular aperture (ϕ 58 mm)
Adapter	SAGE Millimeter, SWC-422F-R1
Isolator	DiTom Microwave, D3I2030
1 st LNA	Low Noise Factory, LNF-LNC15_29A
2 nd LNA	Aldetec, ALM-1826S210
Signal analyzer	Agilent Technologies, N9010A (option 532)

Table 2. Configuration parameters of the signal analyzer

Sweep mode	Fast Fourier Transform
Resolution band width	1 kHz
Window function	Flat-top
Number of points	10001
Scan range	10 MHz from 27.998 GHz, 28.000 GHz, 28.002 GHz (Each of them is divided into two regions because the band width for FFT is 5 MHz.)

plate. The direction of travel of the conversion photon is perpendicular to the plate within 0.06° [12]. The cryogenic receiver measures the intensity of an incoming signal as a function of the frequency [14]. We search for the conversion signal as a narrow peak in the measured spectrum.

The receiver comprises a horn antenna, a waveguide-to-coax adapter, an isolator, two low-noise amplifiers, and a signal analyzer. These components are commercial parts as listed in Table 1. The diameter of the aperture of the conical horn is 58 mm. The antenna has an effective area of $A_{\text{eff}} = 14.8 \text{ cm}^2$ and angular resolution of $\theta_{1/2} = 12.5^\circ$ (full width at half maximum). The calibration is detailed in section 4. We use a cryocooler to maintain the first low-noise amplifier (LNA) at 14 K. The low-temperature condition improves the intrinsic noise of the receiver (i.e., receiver temperature, T_{rec}). T_{rec} is approximately 46 K, which is one order of magnitude better than that under the ambient condition ($T_{\text{rec}} \sim 400 \text{ K}$). Configuration parameters of the signal analyzer are summarized in Table 2.

We assume a Maxwell–Boltzmann distribution (i.e., the standard halo model) for the velocity of the HP-CDM [15]. The distribution function of HP-CDM [16, eq. (15)] is

$$f(\mathbf{v}) = \frac{1}{(\sqrt{\pi}v_c)^3} \exp\left(-\frac{|\mathbf{v} + \mathbf{v}_E|^2}{v_c^2}\right), \quad (2.1)$$

where \mathbf{v} is the velocity of the HP-CDM, v_c is the circular rotation speed of our Galaxy, and \mathbf{v}_E is the velocity of the Earth in the frame of our Galaxy. We can take $|\mathbf{v}_E| \sim v_c$, and the value of $v_c \sim 220 \text{ km/s}$ is adopted by many dark matter search experiments [1, 4, 6, 17–19]. Because the relativistic energy is conserved when HP-CDM is converted to the photon, the velocity of HP-CDM ($v \equiv |\mathbf{v}|$) is transformed to the frequency of the photon (ν) according to

$$h\nu = \frac{h\nu_0}{\sqrt{1 - (v/c)^2}} \quad (h\nu_0 \equiv m_{\gamma'}c^2) \quad \Leftrightarrow \quad v = c\sqrt{1 - \left(\frac{\nu_0}{\nu}\right)^2}. \quad (2.2)$$

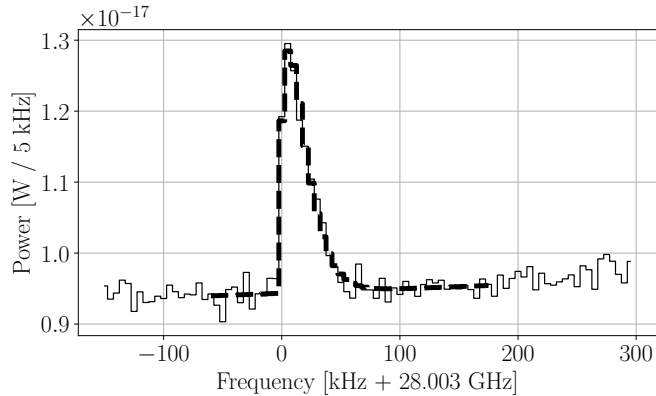


Figure 2. Spectrum obtained in a Monte Carlo simulation assuming $\chi = 2 \times 10^{-9}$ and $\nu_0 = 28.003$ GHz (thin solid line). We measure the signal power by fitting as described in the text of section 5. The fitting result for this simulation is overlaid as a thick dashed line.

Figure 2 shows the simulated spectrum assuming $m_{\gamma'} = 115.81 \mu\text{eV}$ ($\nu_0 = 28.003$ GHz) with the background being a linearly shaped offset. The width of the signal over the peak frequency ($\Delta\nu/\nu_0$) is approximately 10^{-6} .

3 Data set

We recorded data on the rooftop of a building ($36^\circ 8' 53''$ north, $140^\circ 4' 26''$ east, altitude of 40 m above sea level). We set the line of sight of the antenna to the zenith and set the plate above the antenna. An advantage of the system configuration is the reduction of the flux of background radiation striking the antenna. This is because that extra thermal radiation from an outside the field of the plate are dominated by the atmospheric radiation. The power of thermal radiation passing into the receiver (≈ 130 K) is lower than that in the case of ambient radiation (≈ 300 K).

We performed the HP-CDM search from 6 p.m. on the 27th to 6 a.m. on the 28th of October 2016. The measured frequency range is from 27.998 to 28.012 GHz, corresponding to a mass range of 115.79 to 115.85 μeV . There are three scan ranges: 27.998–28.008, 28.000–28.010, and 28.002–28.012 GHz. Each scan range is divided into two regions because the range for the Fourier transformation is 5 MHz. We therefore have six data regions in total for the analysis. Scanning the six regions takes 11 seconds. We repeated this series of scans for a few hours. Each repeated data set is named “run”. There are seven runs in total. We calibrated the receiver gain and noise temperature at the beginning of each run and at the end of the last run.

4 Calibration

Measured signals for each frequency bin are modeled as

$$S(\nu; T_{\text{in}}) = G(\nu)k_{\text{B}} [T_{\text{in}}(\nu) + T_{\text{rec}}(\nu)] \Delta\nu, \quad (4.1)$$

where $G(\nu)$ is the receiver gain at frequency ν , k_{B} is the Boltzmann constant, $T_{\text{in}}(\nu)$ is radiation passing into the receiver with Rayleigh-Jeans unit of Kelvin (K), and $\Delta\nu$ is the

frequency bin width. The calibration uses a blackbody source (ECCOSORB CV-3 from E&C Engineering), which fully covers the aperture of the horn antenna. For each calibration, we recorded two series of data using the blackbody at an ambient temperature ($T_{\text{ambient}} \approx 300$ K) and liquid-nitrogen temperature ($T_{\text{LN}_2} = 77$ K). Using these two data series, we obtain $G(\nu)$ and $T_{\text{rec}}(\nu)$ as

$$G(\nu) = \frac{S(\nu; T_{\text{ambient}}) - S(\nu; T_{\text{LN}_2})}{k_{\text{B}}(T_{\text{ambient}} - T_{\text{LN}_2})\Delta\nu}, \quad (4.2)$$

$$T_{\text{rec}}(\nu) = \frac{S(\nu; T_{\text{LN}_2})}{G(\nu)k_{\text{B}}\Delta\nu} - T_{\text{LN}_2}. \quad (4.3)$$

Table 3 gives results for each calibration. The average gain and noise temperature are approximately 66 dB and 46 K, respectively. Their time variations are less than the uncertainty in the CDM density (7.7%). Through the interpolation of calibration results before and after each run, we measure the power entering the receiver in each frequency bin: $S(\nu)/(G(\nu)\Delta\nu) - k_{\text{B}}T_{\text{rec}}$.

The effective area (A_{eff}) and beam width ($\theta_{1/2}$) of the horn antenna are calibrated using a round-shaped blackbody made by the ECCOSORB AN-72 (E&C Engineering). The blackbody has a diameter of 6 cm; i.e., its area (A_{BB}) is 28.3 cm². We removed the aluminum plate during this calibration. Changing the location of the blackbody in the ambient, we measured powers at each location. In each step, we also measured the atmospheric radiation without the blackbody. We recorded calibration data on October 24th and 26th. The ambient temperatures were 299 K on the 24th and 302 K on the 26th. We measured $G(\nu)$ and $T_{\text{rec}}(\nu)$ before and after calibration on each day. The distribution of the measured power is modeled with a Gaussian beam shape [20],

$$\frac{A_{\text{eff}} \cos(\theta_{\text{BB}}) \cdot A_{\text{BB}} \nu^2}{L^2 c^2} \times \exp\left[-2\frac{(x-x_0)^2 + (y-y_0)^2}{w^2}\right] \times k_{\text{B}}(T_{\text{BB}} - T_{\text{atm}}) \left(\tan(\theta_{\text{BB}}) = \frac{\sqrt{(x-x_0)^2 + (y-y_0)^2}}{L}, \quad w = \frac{2L}{\sqrt{2 \log 2}} \tan(\theta_{1/2}/2) \right), \quad (4.4)$$

where (x, y) is the location of the blackbody, (x_0, y_0) is the line of sight, θ_{BB} is the direction of the blackbody with respect to the line of sight, w is the beam size on the plane of the blackbody, T_{BB} is the blackbody temperature in the ambient, T_{atm} is the atmospheric

Table 3. Receiver gains and receiver temperatures measured soon before each run and after the last run. Here, $\langle G \rangle$ and $\langle T_{\text{rec}} \rangle$ are the average gain and receiver temperature in the six frequency regions.

Date time	$\langle G \rangle$ [dB]	$\langle T_{\text{rec}} \rangle$ [K]	T_{ambient} [K]
October 27th 18:36	65.67 ± 0.02	48.2 ± 0.3	290.3
19:40	65.78 ± 0.04	46.4 ± 0.3	289.5
21:36	66.01 ± 0.03	45.9 ± 0.3	288.4
23:43	66.13 ± 0.02	45.7 ± 0.3	287.3
October 28th 02:05	66.57 ± 0.02	45.4 ± 0.4	284.8
03:05	66.78 ± 0.02	45.2 ± 0.3	283.6
04:05	66.81 ± 0.02	45.9 ± 0.4	283.8
05:32	66.93 ± 0.03	45.2 ± 0.5	283.8

Table 4. A_{eff} and $\theta_{1/2}$ for each frequency region on each day.

Date	Frequency [GHz]	A_{eff} [cm ²]	$\theta_{1/2}$ [°]	x_0 [mm]	y_0 [mm]
October 24th	27.998–28.003	14.6 ± 0.5	13.3 ± 0.6	-67.9 ± 3.8	-10.9 ± 3.7
	28.000–28.005	14.4 ± 0.5	12.5 ± 0.5	-65.7 ± 3.6	2.6 ± 3.5
	28.002–28.007	14.8 ± 0.5	12.9 ± 0.5	-60.9 ± 3.6	-12.9 ± 3.6
	28.003–28.008	15.0 ± 0.5	12.8 ± 0.5	-55.9 ± 3.5	-10.2 ± 3.5
	28.005–28.010	15.9 ± 0.5	12.0 ± 0.4	-69.8 ± 3.3	-11.1 ± 3.2
	28.007–28.012	15.5 ± 0.5	12.5 ± 0.5	-55.1 ± 3.4	-12.4 ± 3.4
October 26th	27.998–28.003	13.6 ± 0.6	13.5 ± 0.7	-64.6 ± 4.9	1.1 ± 4.7
	28.000–28.005	14.1 ± 0.6	12.6 ± 0.6	-77.3 ± 4.7	-7.1 ± 4.4
	28.002–28.007	14.1 ± 0.6	13.6 ± 0.7	-80.7 ± 5.2	0.6 ± 4.7
	28.003–28.008	15.5 ± 0.6	12.5 ± 0.6	-72.3 ± 4.2	1.3 ± 3.9
	28.005–28.010	14.6 ± 0.6	13.8 ± 0.7	-77.1 ± 5.1	-8.3 ± 4.7
	28.007–28.012	16.8 ± 0.7	11.1 ± 0.4	-71.3 ± 3.5	-3.5 ± 3.4

radiation temperature, and L is the distance from the horn antenna to the calibration source (1030 mm).

For each calibration, we obtain A_{eff} , $\theta_{1/2}$, and (x_0, y_0) by fitting with eq. (4.4) as shown in Figure 3. Fitting results for each calibration are summarized in Table 4. By taking a weighted average, we obtain $A_{\text{eff}} = 14.8 \pm 0.9 \text{ cm}^2$ and $\theta_{1/2} = 12.5 \pm 0.2^\circ$. We here assign errors as the square root of the quadrature sum of the deviation among calibrations, uncertainties for the gain, T_{rec} , T_{BB} , A_{BB} , and T_{atm} .

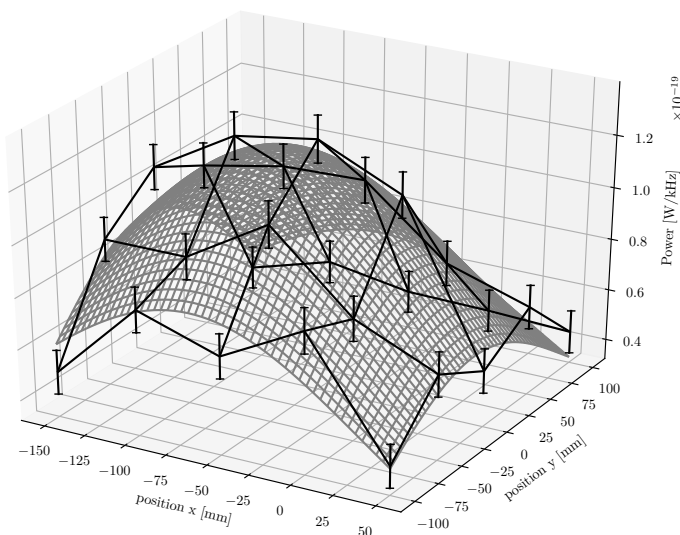


Figure 3. Measured powers with changing blackbody location. We obtain the beam shape and power at the beam center through fitting. We take these calibration data for each frequency region.

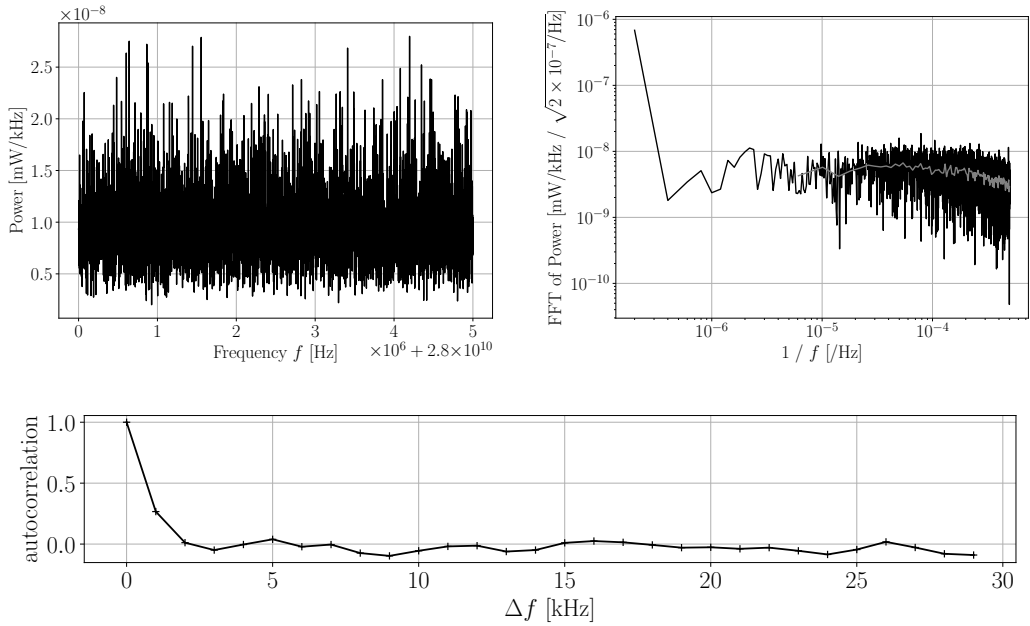


Figure 4. [top-left] Example of the power measured by the spectrometer. The bin width is 1 kHz and there are 5000 samples in each frequency region. [top-right] The Fourier-transformed spectrum of measured powers. The gray line shows the average. White noise generates a flat structure in the region between $\mathcal{O}(1 \times 10^{-5})$ and $\mathcal{O}(1 \times 10^{-4})$ /Hz. A cut-off due to correlation between adjacent bins is seen above $\mathcal{O}(1 \times 10^{-4})$ /Hz. [bottom] Autocorrelation of the raw data shown at top-left.

5 Analysis

We search for the HP-CDM signal in frequency spectra for each run in each frequency region by fitting with a model function with changing ν_0 . Before fitting, we re-bin the power spectra to eliminate systematic bias from correlation between adjacent frequency bins. Figure 4 shows measured powers as a function of frequency, a Fourier-transformed spectrum, and the correlation among bins. We find correlation among neighboring bins up to 3 kHz. We thus use a frequency bin width of 5 kHz by summing for five samples.

We fit signal powers by changing ν_0 in steps of 5 kHz. A fitting function comprises the signal term and background terms. We model the background shape with a first-order polynomial,

$$f(\nu; P_{\gamma'}, \nu_0, a, b) = P_{\gamma'} \{F(\nu + 2.5 \text{ kHz}; \nu_0) - F(\nu - 2.5 \text{ kHz}; \nu_0)\} + a(\nu - \nu_0) + b, \quad (5.1)$$

where $P_{\gamma'}$ is the power of the conversion photon, and cumulative distribution $F(\nu; \nu_0)$ is introduced to account for the effect of finite bin width. Cumulative distribution of HP-CDM

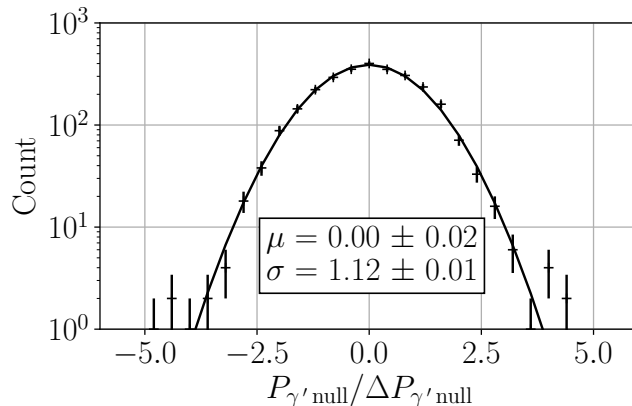


Figure 5. Distribution of $P_{\gamma' \text{ null}}/\Delta P_{\gamma' \text{ null}}$ for the null samples. Fitting results obtained with the Gaussian distribution are also shown.

velocity $F_v(v)$ is

$$\begin{aligned}
 F_v(v) &= \int_0^v dv' \int^{4\pi} d\Omega f(\mathbf{v}') v'^2 \\
 &= \frac{v_c}{2\sqrt{\pi}v_E} \left\{ \exp \left[- \left(\frac{v + v_E}{v_c} \right)^2 \right] - \exp \left[- \left(\frac{v - v_E}{v_c} \right)^2 \right] \right\} \\
 &\quad + \frac{1}{2} \left\{ \operatorname{erf} \left[\frac{v - v_E}{v_c} \right] + \operatorname{erf} \left[\frac{v + v_E}{v_c} \right] \right\}, \tag{5.2}
 \end{aligned}$$

$$\operatorname{erf}(x) = \frac{2}{\sqrt{\pi}} \int_0^x e^{-t^2} dt. \tag{5.3}$$

Plugging eq. (2.2) into eq. (5.2), we obtain $F(\nu; \nu_0)$. For each fit, we use a fitting range of 240 kHz (48 bins): $(\nu_0 - 60 \text{ kHz}) - (\nu_0 + 180 \text{ kHz})$. We estimate the error in each bin as white noise and assume it has the same size among bins. We apply the Fourier transform to the frequency spectra as shown in Figure 4 [top-right]. We calculate the mean in the “1 / frequency” region between $6 \times 10^{-5} / \text{Hz}$ and $1 \times 10^{-4} / \text{Hz}$ and use it as the white-noise error.

We validate the analysis procedure adopting a “null sample” method. We randomly divide the calibrated data for each run into two data sets, and we create subtracted data samples for each region (named null samples). No signal is contained in a null sample because signals in each data set cancel out. We check whether the mean value of the fitting results for null samples ($P_{\gamma' \text{ null}}$) is consistent with a value of zero. We also check for analysis bias between the fitting error ($\Delta P_{\gamma' \text{ null}}$) and a standard deviation of fitting results. Figure 5 shows the distribution of $P_{\gamma' \text{ null}}/\Delta P_{\gamma' \text{ null}}$. The distribution is fitted using a Gaussian curve, yielding a mean ($\mu = 0.00 \pm 0.02$) and a standard deviation ($\sigma = 1.12 \pm 0.01$). No bias is found for the mean value. However, we understand that the error used in the signal extraction should be corrected using a multiplication factor of 1.12. The raw fitting error is deemed inaccurate because we only consider white noise in the fitting. An imperfection of the background model may also have this effect.

Systematic uncertainties are summarized in Table 5. A small angle offset of the conversion photons ($< 0.06^\circ$) slightly reduces the detection efficiency. This efficiency loss is

Table 5. Systematic uncertainties of the HP-CDM signal.

Source	%
Angular dispersion of HP-CDM	0.7
Alignment, flatness, roughness, and reflectivity of the aluminum plate	3.2
Effective area of antenna (A_{eff})	5.8
Responsivity of the receiver	7.7
Frequency response	0.9
Frequency bin	4.8
Total	11.3

estimated from the beam width: $1 - \exp[-0.06^\circ/(12.25^\circ/2) \cdot \log(2)] = 0.7\%$. Meanwhile, plate curvature, roughness, reflectivity, and the misalignment of the plate direction result in a loss of signal. In particular, plate curvature (i.e., deviation from flatness) results in non-negligible loss. Plate curvature occurs because the aluminum plate is held at its edges and deforms under its own weight. The deformation of the plate is measured using a ruler and the curvature is estimated as $R = 62.5$ m conservatively. This gives uncertainty of 3.2%. Systematic uncertainty in A_{eff} is determined by the calibration error described in section 4. We understand that the receiver gain is stable compared with the uncertainty in CDM density (7.7%) as described in section 4. The frequency stability is examined using a vector network analyzer (VNA, Agilent, N5224A) as a microwave source. The VNA generates a monochrome wave with a frequency of 28.003 GHz, and the signal analyzer measures the wave. We confirm that the fluctuation of the frequency peak position is below 1 kHz even if we change the temperature of the signal analyzer from 27.8 °C to 40.3 °C. This effect corresponds to a tiny efficiency loss of 0.9%. A possible fitting bias due to the frequency bin is estimated using the Monte Carlo simulation: 4.8%. The total systematic uncertainty is assigned to be 11.3% for signal detection.

6 Results

Figure 6 shows the extracted power ($P_{\gamma'}$) and statistical error ($\Delta P_{\gamma'}$) as functions of frequency. Local p -values, $(1 - \text{erf}(P_{\gamma'}/\Delta P_{\gamma'}/\sqrt{2}))/2$, are also shown. We apply the correction for statistical error (i.e., a multiplication of 1.12) as described in the previous section. The minimum local p -value in 2752 frequency bins is $p_{\text{min}} = 1.24 \times 10^{-4}$ (3.7σ). Adopting the methodology described in ref. [21], we account for the look elsewhere effect. We determine the number of independent frequency windows (1.0×10^3) by conducting Monte Carlo simulations. The probability of exceeding p_{min} in any frequency bin is estimated as

$$1 - (1 - p_{\text{min}})^{1.0 \times 10^3} = 0.12 \quad (1.2\sigma). \quad (6.1)$$

We do not find any significant excess of the HP-CDM signal from zero.

We calculate limits of power at the 95% confidence level for each frequency bin using

$$\max(0, P_{\gamma'}) + 1.65\Delta P_{\gamma'}. \quad (6.2)$$

Adopting eq. (1.3), we set upper limits for the mixing angle as shown in Figure 7. Obtained limits are $\chi < 1.8\text{--}4.3 \times 10^{-10}$ at the 95% confidence level. This is the most stringent limit obtained to date in the considered mass range.

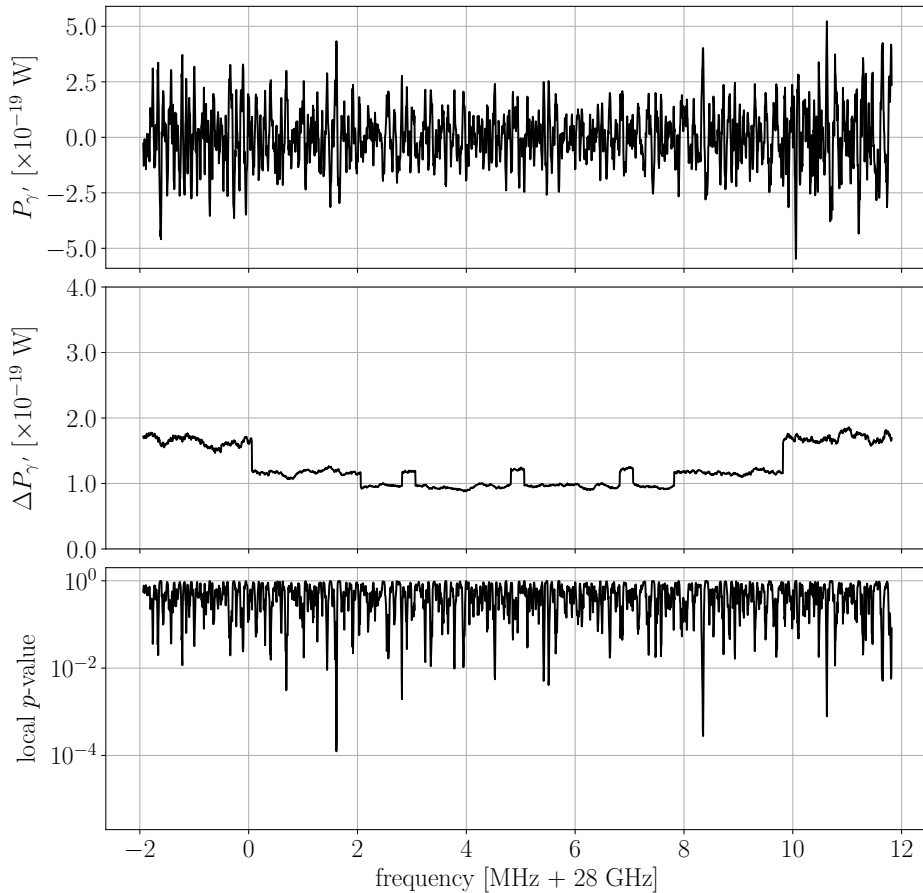


Figure 6. Extracted powers for the HP-CDM signal as a function of frequency [top], statistical errors [middle], and local p-values [bottom].

7 Conclusions

We searched for HP-CDM in the mass region of $115.79\text{--}115.85\ \mu\text{eV}$ using a metal plate as the photon converter and cryogenic receiver as a photon detector in the millimeter wave range. No excess from the zero-signal hypothesis was found in this region. We set upper limits, $\chi < 1.8\text{--}4.3 \times 10^{-10}$, at the 95% confidence level.

Acknowledgments

This work is supported by JSPS KAKENHI under grant numbers 16K13809 and 19H05499, JST START (Program for Creating START-ups from Advanced Research and Technology), and the Special Postdoctoral Researchers Program in RIKEN. We thank M. Hasegawa and Y. Minami for comments on the draft, and Glenn Pennycook, MSc, from Edanz Group (<https://en-author-services.edanzgroup.com/>) for editing a draft of this manuscript.

References

- [1] THE DARKSIDE COLLABORATION, P. Agnes, I. F. M. Albuquerque, T. Alexander, A. K. Alton,

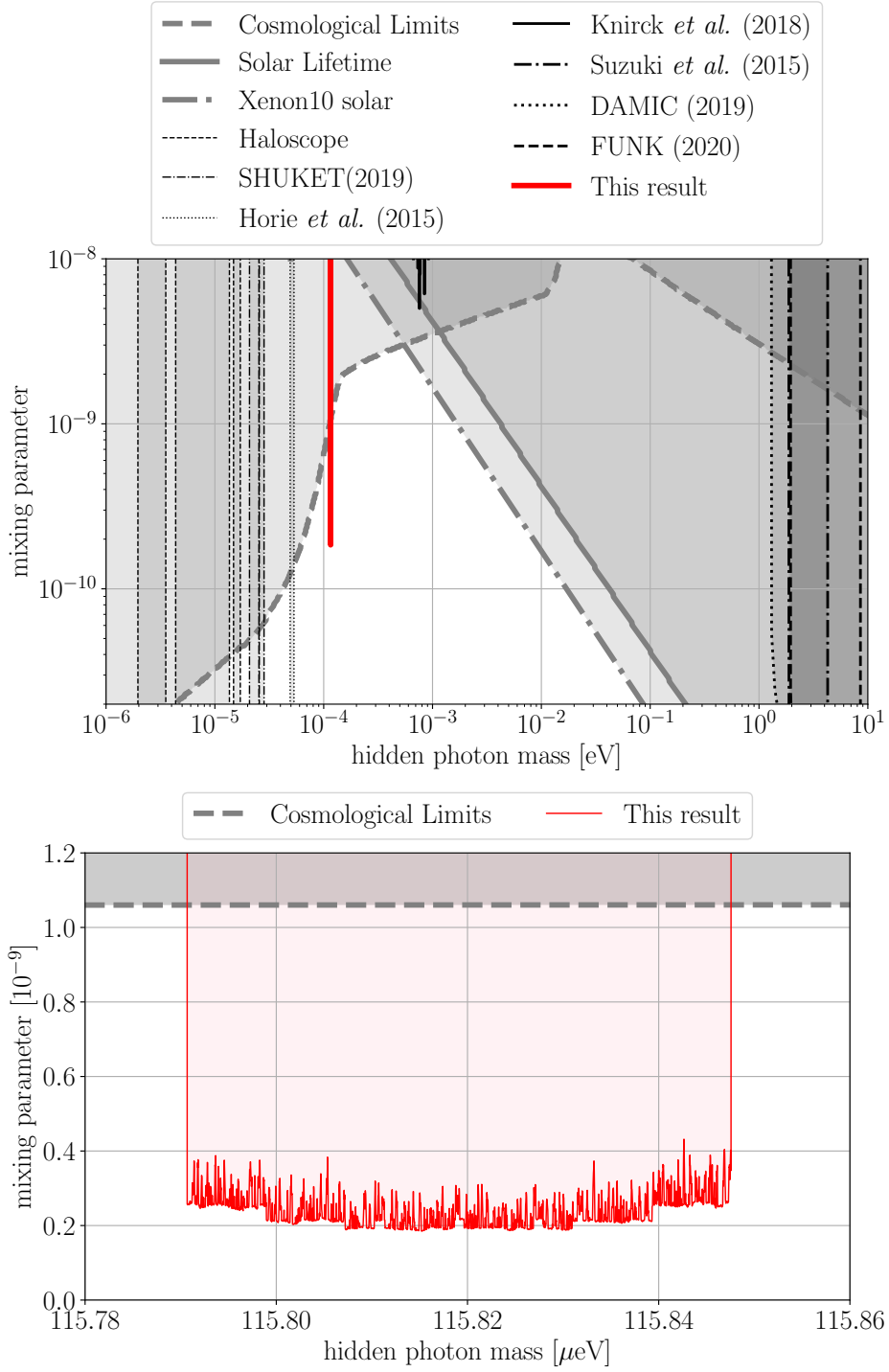


Figure 7. Constraints of the kinetic mixing parameter as a function of the HP-CDM mass. Shaded areas are the excluded parameter space. The bottom plot having a linear scale is an expanded view of the top plot around the mass region searched in the present paper. Results of previous research are also shown [7, 12, 22–29]. We set the most stringent limits in the mass range from 115.79 to 115.85 μeV .

- G. R. Araujo, D. M. Asner et al., *Constraints on sub-gev dark-matter–electron scattering from the darkside-50 experiment*, *Phys. Rev. Lett.* **121** (2018) 111303, [[1802.06998](#)].
- [2] DEAP-3600 COLLABORATION, P.-A. Amaudruz, M. Baldwin, M. Batygov, B. Beltran, C. E. Bina, D. Bishop et al., *First results from the deap-3600 dark matter search with argon at snolab*, *Phys. Rev. Lett.* **121** (2018) 071801, [[1707.08042](#)].
- [3] SUPERCDMS COLLABORATION, R. Agnese, A. J. Anderson, T. Aramaki, I. Arnquist, W. Baker, D. Barker et al., *Projected sensitivity of the supercdms snolab experiment*, *Phys. Rev. D* **95** (2017) 082002, [[1610.00006](#)].
- [4] LUX COLLABORATION, D. S. Akerib, S. Alsum, H. M. Araújo, X. Bai, A. J. Bailey, J. Balajthy et al., *Results from a search for dark matter in the complete lux exposure*, *Phys. Rev. Lett.* **118** (2017) 021303, [[1608.07648](#)].
- [5] E. Aprile, J. Aalbers, F. Agostini, M. Alfonsi, F. D. Amaro, M. Anthony et al., *Physics reach of the XENON1t dark matter experiment.*, *JCAP* **2016** (2016) 027–027, [[1512.07501](#)].
- [6] PANDAX-II COLLABORATION, C. Fu, X. Cui, X. Zhou, X. Chen, Y. Chen, D. Fang et al., *Spin-dependent weakly-interacting-massive-particle–nucleon cross section limits from first data of pandax-ii experiment*, *Phys. Rev. Lett.* **118** (2017) 071301, [[1611.06553](#)].
- [7] P. Arias, D. Cadamuro, M. Goodsell, J. Jaeckel, J. Redondo and A. Ringwald, *WISPy cold dark matter*, *JCAP* **06** (2012) 013, [[1201.5902](#)].
- [8] J. Jaeckel, *A force beyond the Standard Model - Status of the quest for hidden photons*, *Frascati Phys. Ser.* **56** (2012) 172–192, [[1303.1821](#)].
- [9] J. Jaeckel and A. Ringwald, *A cavity experiment to search for hidden sector photons*, *Physics Letters B* **659** (2008) 509 – 514, [[0707.2063](#)].
- [10] A. Wagner, G. Rybka, M. Hotz, L. J. Rosenberg, S. J. Asztalos, G. Carosi et al., *Search for hidden sector photons with the admx detector*, *Phys. Rev. Lett.* **105** (2010) 171801, [[1007.3766](#)].
- [11] D. Horns, J. Jaeckel, A. Lindner, A. Lobanov, J. Redondo and A. Ringwald, *Searching for WISPy cold dark matter with a dish antenna*, *JCAP* **1304** (2013) 016, [[1212.2970](#)].
- [12] J. Suzuki, Y. Inoue, T. Horie and M. Minowa, *Hidden photon CDM search at Tokyo*, in *11th Patras Work. Axions, WIMPs and WISPs*, 2015. [1509.00785](#). DOI.
- [13] R. Catena and P. Ullio, *A novel determination of the local dark matter density*, *JCAP* **08** (2010) 004, [[0907.0018](#)].
- [14] O. Tajima, K. Araki, H. Ishimoto and T. Nagasaki, *Sensing of the atmospheric water vapor with millimeter wave spectrometer — KUMODES*, *2016 Prog. Electromagn. Res. Symp.* (2016) 4157–4161.
- [15] C. A. J. O’Hare and A. M. Green, *Axion astronomy with microwave cavity experiments*, *Phys. Rev. D* **95** (2017) 063017, [[1701.03118](#)].
- [16] A. K. Drukier, K. Freese and D. N. Spergel, *Detecting cold dark-matter candidates*, *Phys. Rev. D* **33** (1986) 3495–3508.
- [17] CDMS-II, CDMS, Z. Ahmed et al., *Search for inelastic dark matter with the CDMS II experiment*, *Phys. Rev. D* **83** (2011) 112002, [[1012.5078](#)].
- [18] XENON, E. Aprile et al., *Dark Matter Search Results from a One Ton-Year Exposure of XENON1T*, *Phys. Rev. Lett.* **121** (2018) 111302, [[1805.12562](#)].
- [19] LUX-ZEPLIN, D. Akerib et al., *Projected WIMP sensitivity of the LUX-ZEPLIN dark matter experiment*, *Phys. Rev. D* **101** (2020) 052002, [[1802.06039](#)].
- [20] P. F. Goldsmith, *Quasi-optical techniques*, *Proceedings of the IEEE* **80** (1992) 1729–1747.

- [21] J. W. Foster, N. L. Rodd and B. R. Safdi, *Revealing the dark matter halo with axion direct detection*, *Phys. Rev. D* **97** (2018) 123006, [[1711.10489](#)].
- [22] H. An, M. Pospelov and J. Pradler, *New stellar constraints on dark photons*, *Phys. Lett. B* **725** (2013) 190–195, [[1302.3884](#)].
- [23] J. Redondo and G. Raffelt, *Solar constraints on hidden photons re-visited*, *JCAP* **08** (2013) 034, [[1305.2920](#)].
- [24] J. Suzuki, *Experimental search for hidden photon CDM in the eV mass range with a dish antenna*, *JCAP* **09** (2015) 042, [[1504.00118v1](#)].
- [25] I. M. Bloch, R. Essig, K. Tobioka, T. Volansky and T.-T. Yu, *Searching for dark absorption with direct detection experiments*, *J. High Energ. Phys.* **2017** (2017) 087, [[1608.02123](#)].
- [26] S. Knirck, T. Yamazaki, Y. Okesaku, S. Asai, T. Idehara and T. Inada, *First results from a hidden photon dark matter search in the meV sector using a plane-parabolic mirror system*, *JCAP* **11** (2018) 031–031, [[1806.05120](#)].
- [27] P. Brun, L. Chevalier and C. Flouzat, *Direct searches for hidden-photon dark matter with the shuket experiment*, *Phys. Rev. Lett.* **122** (2019) 201801, [[1905.05579](#)].
- [28] DAMIC COLLABORATION, A. Aguilar-Arevalo, D. Amidei, D. Baxter, G. Canelo, B. A. Cervantes Vergara, A. E. Chavarria et al., *Constraints on light dark matter particles interacting with electrons from damic at snolab*, *Phys. Rev. Lett.* **123** (2019) 181802, [[1907.12628](#)].
- [29] FUNK EXPERIMENT, A. Andrianavalomahefa et al., *Limits from the Funk Experiment on the Mixing Strength of Hidden-Photon Dark Matter in the Visible and Near-Ultraviolet Wavelength Range*, [2003.13144](#).